Journal of Colloid and Interface Science 674 (2024) 753–765

Contents lists available at ScienceDirect

Journal of Colloid And Interface Science

journal homepage: www.elsevier.com/locate/jcis

Bioengineered self-assembled nanofibrils for high-affinity SARS-CoV-2 capture and neutralization

Molood Behbahanipour, Susanna Navarro, Oriol Bárcenas, Javier Garcia-Pardo, Salvador Ventura *

Institut de Biotecnologia i de Biomedicina (IBB) and Departament de Bioquímica i Biologia Molecular; Universitat Autònoma de Barcelona, 08193 Bellaterra (Barcelona), Spain

HIGHLIGHTS

- Modular bioengineered nanofibrils neutralize SARS-CoV-2 virus-like particles.
- Recombinant protein subunits spontaneously assemble into functional fibrils.
- The assembled amyloid-like nanofibrils are biocompatible.
- Mesoscopic structure and activity of the protein assembly are easily modulated.
- Surfaces coated with nanofibrils capture SARS-CoV-2 Spike in wet environments.

GRAPHICAL ABSTRACT

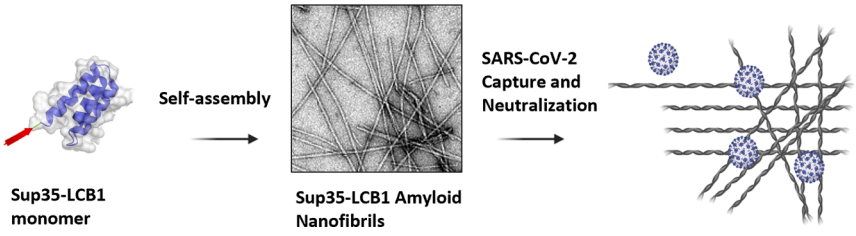

ARTICLE INFO

Keywords:
Amyloid Fibrils
SARS-CoV-2
Supramolecular Assemblies
Antiviral Biomaterials
Functional Polymers

ABSTRACT

The recent coronavirus disease 2019 (COVID-19) pandemic caused by the severe acute respiratory syndrome coronavirus 2 (SARS-CoV-2) has spurred intense research efforts to develop new materials with antiviral activity. In this study, we genetically engineered amyloid-based nanofibrils for capturing and neutralizing SARS-CoV-2. Building upon the amyloid properties of a short Sup35 yeast prion sequence, we fused it to SARS-CoV-2 receptor-binding domain (RBD) capturing proteins, LCB1 and LCB3. By tuning the reaction conditions, we achieved the spontaneous self-assembly of the Sup35-LCB1 fusion protein into a highly homogeneous and well-dispersed amyloid-like fibrillar material. These nanofibrils exhibited high affinity for the SARS-CoV-2 RBD, effectively inhibiting its interaction with the angiotensin-converting enzyme 2 (ACE2) receptor, the primary entry point for the virus into host cells. We further demonstrate that this functional nanomaterial entraps and neutralizes SARS-CoV-2 virus-like particles (VLPs), with a potency comparable to that of therapeutic antibodies. As a proof of concept, we successfully fabricated patterned surfaces that selectively capture SARS-CoV-2 RBD protein on wet environments. Collectively, these findings suggest that these protein-only nanofibrils hold promise as disinfecting coatings endowed with selective SARS-CoV-2 neutralizing properties to combat viral spread or in the development of sensitive viral sampling and diagnostic tools.

Abbreviations: COVID-19, coronavirus disease 2019; SARS-CoV-2, severe acute respiratory syndrome coronavirus 2; RBD, receptor-binding domain; ACE2r, angiotensin-converting enzyme 2 receptor; VLPs, virus-like particles; S protein, viral spike protein; SAC, soft amyloid core; IC_{50}, half-maximal inhibitory concentration; CD, circular dichroism; Na-PB, sodium phosphate buffer; BCA, bicinchoninic acid assay; Th-T, thioflavin T; CR, congo red; ATR-FTIR, attenuated total reflectance Fourier-transform infrared; NS-TEM, Negative-Stain Transmission Electron Microscopy; SDS, sodium dodecyl sulfate; APRs, regions prone to aggregation; SD, standard deviation; RT, room temperature; PVDF, polyvinylidene difluoride; PPI, protein–protein interaction.

* Corresponding author.
E-mail addresses: Molood.Behbahanipour@uab.cat (M. Behbahanipour), Susanna.Navarro.Cantero@uab.cat (S. Navarro), Oriol.Barcenas@uab.cat (O. Bárcenas), Javiergarciapardo@msn.com (J. Garcia-Pardo), Salvador.Ventura@uab.cat (S. Ventura).

https://doi.org/10.1016/j.jcis.2024.06.175
Received 19 February 2024; Received in revised form 10 June 2024; Accepted 23 June 2024
Available online 24 June 2024

1. Introduction

The coronavirus disease 2019 (COVID-19) pandemic has sparked an unprecedented global research effort to combat the severe acute respiratory syndrome coronavirus 2 (SARS-CoV-2). This multifaceted crusade encompasses a diverse array of antiviral strategies aimed at mitigating disease severity, including the development of vaccines [1], antiviral drugs [2,3], convalescence plasma therapy [4,5], RNA interference [6,7], or prophylactic measures [8]. Despite all these concerted efforts, SARS-CoV-2 has caused over 6.9 million deaths since its emergence in December 2019 (~2.0 % fatality rate) [9], stressing the need for innovative approaches to address the evolving complexities of the disease. One major challenge is the rapid environmental transmission of the SARS-CoV-2, which is primarily mediated through respiratory droplets and aerosols. Recent studies have shown that the virus contained in these droplets can persist on surfaces for several days, enabling its spread through direct contact with contaminated surfaces and subsequent self-inoculation *via* touching the eyes, nose, and mouth [10–12].

Once SARS-CoV-2 reaches the host cell, a critical step for successful viral internalization in human cells is the attachment of the receptor binding domain (RBD) from the viral spike (S) protein to the angiotensin-converting enzyme 2 receptor (ACE2r), which is highly expressed in various SARS-CoV-2 target tissues, including the lungs, heart, and gastrointestinal tract [13–16]. Different strategies have been devised to disrupt this critical interaction, including the use of small chemical molecules [17], peptide inhibitors [18], monoclonal antibodies [19–22], or oligomeric nanomaterials [23] that specifically target the SARS-CoV-2 spike protein, thereby blocking its ability to bind to ACE2r and preventing viral spread.

Despite the aforementioned advances, the high transmission rates of SARS-CoV-2 and the rapid emergence of resistant strains that evade current treatments or vaccines underscore the importance of prevention in combating COVID-19 [24,25]. Consequently, the development of new coatings, designed to act as antiviral barriers against the spread of SARS-CoV-2 through fluids, is gaining traction. Various materials, such as polymers, metals (*i.e.* Cu or Zn), metal oxides (CuO, ZnO or TiO_2), and their corresponding nanoparticles, have been investigated for developing antiviral coatings on different surfaces [8,26–29]. However, these conventional approaches are often non-selective and exhibit significant toxicity [28,30,31]. As a result, alternative biomaterials with antiviral properties are being investigated [23].

Amyloid-inspired fibrils have emerged as a cost-effective and sustainable way to produce versatile biocompatible nanomaterials [32–34] with a wide range of applications, including tissue engineering [35], pH sensors [36] or synthetic catalysts [32]. These protein-based materials typically feature densely packed amyloid cores formed by hydrogen-bonded β-sheets [34,37–39]. This distinctive supramolecular architecture provides a strong internal bonded network, translating into remarkable material properties, including high Young's modulus and tensile strength [40] and, often, remarkable resistance to chemical and proteolytic degradation [41]. A key advantage of these self-assembling materials lies in the ability to incorporate specific functionalities through straightforward protein engineering techniques [42,43].

Herein, we have engineered a novel biocompatible protein material for the targeted capture and neutralization of SARS-CoV-2 using self-assembling amyloid-based nanofibrils. We exploited the self-assembly of the Sup35 yeast prion soft amyloid core (Sup35-SAC) [44], fused to two different SARS-CoV-2 RBD-binding moieties, namely LCB1 and LCB3 [45]. These globular small α-helical domains, originally designed by David Baker's lab [45], have been exploited by our group [23] and others [46–48] to generate novel molecules that bind to SARS-CoV-2 spike protein. Using a modular approach and tailoring the self-assembly conditions, we obtained a set of Sup35-LCB1/LCB3 nanofibrils with diverse supramolecular morphologies and activities. Computational modelling and experimental data indicate that Sup35-LCB1 nanofibrils possess an amyloid-like architecture. As intended, they are non-toxic and display functional binding surfaces. Accordingly, they effectively recognize SARS-CoV-2 RBD, with a half-maximal inhibitory concentration (IC_{50}) as low as ~ 6 ng/mL. The high density of binding motifs at the fibrils surface confers avidity, enabling them to neutralize the fusion of SARS-CoV-2 virus-like particles (VLPs) to the membrane of ACE2r-expressing human cells with exceptional potency. As proof-of-concept material, the Sup35-LCB1 nanofibrils were embedded in a PVDF matrix, resulting in an amyloid-based surface coating with remarkable efficacy and selectivity in trapping SARS-CoV-2 RBD.

Overall, this study introduces a novel, protein-only fibrillar nanomaterial designed to block SARS-CoV-2 spreading, demonstrating potential as an effective biocompatible antiviral surface coating.

2. Materials and methods

2.1. Protein expression and purification

To engineer constructs that express the Sup35-LCB1/3 proteins, the cDNAs encoding the LCB1 and LCB3 protein sequences were inserted into a pET28a vector. Both proteins were fused to the C-terminus of the 21-residue-long soft amyloid core of Sup35 yeast prion protein through a flexible (SGSGS) linker. Additionally, an 6x His-tag was also added to the C-terminus to facilitate nickel affinity purification. For protein expression, BL21 (DE3) *E. coli* cells were transformed with the plasmids and grown overnight in LB medium containing 50 μg/mL kanamycin. After incubation overnight at 37 °C under constant agitation, the cultures were diluted (1:100) in fresh LB medium and grown until reaching a culture with an optical density (600 nm) of 0.4. Then, Sup35-LCB1/3 expression was induced by adding 1 mM IPTG, followed by incubation at 20 °C overnight. The cells were then collected and lysed by sonication on ice in 30 mL lysis buffer (20 mM sodium phosphate buffer (Na-PB) pH 8.0, 0.3 M NaCl, 1 mM PMSF, 1 μg/mL DNase, and EDTA-free protease inhibitor Mini Tablets) per L of culture. Subsequently, cell lysates were centrifuged at 20000 rpm for 30 min at 4 °C, and the clarified supernatants were filtered through 0.45 μm low protein binding filters. The filtered samples were loaded onto a pre-equilibrated HisTrap™ FF crude column (Cytiva), previously washed with 10 column volumes (CV) of equilibration buffer (20 mM Na-PB pH 8.0, 0.5 M NaCl with 20 mM imidazole). The recombinant proteins were eluted by applying a gradient (5 CV) of the elution buffer (20 mM Na-PB pH 8.0, 0.5 M NaCl, and 0.5 M imidazole). The eluted recombinant proteins were pooled and further purified using a size exclusion chromatography in a Superdex 75 increase 10/300 GL column (GE Healthcare, USA) and 20 mM sodium phosphate pH 8.0 buffer (Na-PB). Finally, the purified proteins were flash-frozen in liquid nitrogen and kept at −80 °C until use. The purity of the purified Sup35-LCB1/3 samples was confirmed by SDS-PAGE analysis. The final protein concentrations were determined with the bicinchoninic acid (BCA) assay (Thermo Fisher Scientific, Waltham, Massachusetts, USA).

2.2. Circular dichroism (CD) spectroscopy

The far-UV CD spectra for soluble Sup35-LCB1 and Sup35-LCB3 proteins were measured in the 200–260 nm wavelength range using a Jasco J-815 CD spectropolarimeter. The samples were diluted at a concentration of 40 μM in 20 mM Na-PB buffer at pH 8 and 25 °C. The measurements were taken with a data pitch of 0.2 nm, a bandwidth of 1 nm, and 20 accumulations at a scanning speed of 100 nm/min. To follow the changes in the CD signal during the aggregation reaction for both Sup35-LCB1 and Sup35-LCB3, we measured the CD spectrum of 20 μM samples on days 0, 3, and 6. This was done under three different Na-PB conditions.

2.3. Formation of protein nanofibrils

Fibrillation reactions for Sup35-LCB1 and Sup35-LCB3 were carried out at final protein concentration of 500 μM (5.28 mg/mL). Prior to the reaction, samples were filtered through 0.22 μm low protein binding filters and then immediately diluted in Na-PB at three different concentrations (20 mM, 150 mM, or 300 mM), at pH of 8.0 or in double-distilled Milli-Q™ water. The solutions were incubated at 37 °C with agitation at 600 rpm for 6 days. Afterwards, they were centrifuged for 1 h at 16000 g at 10 °C to separate insoluble fibrils from the soluble supernatant. The final protein concentrations in the supernatant were determined by the BCA assay and subtracted from the initial protein concentration (500 μM, 5.28 mg/mL) to estimate the amount of protein present in the amyloid fibrils after the incubation reaction.

2.4. Amyloid dye binding

The Sup35-LCB1/3 self-assembly into amyloid fibril at different salt concentration was evaluated using Thioflavin-T (Th-T) and Congo red (CR) dye binding assays. ThT fluorescence of the soluble protein and the self-assembled amyloid fibrils were assayed at a final protein concentration of 0.2 mg/mL and in the presence of 25 μM ThT. The fluorescence of these samples was recorded in the 460 to 600 nm range upon excitation at 445 nm using a Jasco FP-8200 spectrofluorometer (Jasco Corporation, Japan) (excitation/emission bandwidth of 5 nm).

CR spectral shift assays were performed using a SPECORD® 200 Plus spectrophotometer (Analytik Jena, Germany) to measure the absorption spectrum in the visible region (375–700 nm) for amyloid fibril suspensions (0.2 mg/mL) in the presence of the 20 μM CR dye. To determine the CR signal specific to protein binding, the absorption spectrum of only proteins was subtracted from that of proteins bound to CR. Buffers without protein were also evaluated as negative controls for both Th-T and CR assays.

2.5. Fourier transform infrared (FTIR) spectroscopy

Infrared spectra of fibrils formed in different salt conditions were collected using Bruker Tensor 27 FTIR spectrometer (Bruker Optics, USA) supplied with a Specac Golden Gate MKII ATR accessory. 50 μL of each fibril suspension was centrifuged for 1 h at 16100 g at 10 °C. Then, the pellet was resuspended in 10 μL Milli-Q water and placed on the diamond ATR crystal. Before analysis, the solvent was evaporated by using a stream of nitrogen. FTIR spectrum of all the samples was recorded between 1700 and 1600 cm^{-1} by performing 32 acquisitions at a resolution of 1 cm^{-1}. In all the cases, the spectra were corrected to remove background absorption. OPUS MIR Tensor 27 software (Bruker Optics, USA) was used for data normalization with the Min/Max normalization method. IR spectra were fitted employing automated peak fitting using the "AutoFit Peaks I Residuals" option with the "vary widths" condition for the autoscan procedure, until reaching iteration 7 and an $r^2 > 0.997$ using PeakFit package v4.12 (Systat Software, San Jose, CA). The area for each Gaussian curve was calculated in the amide I region from 1700 to 1600 cm^{-1} using the second derivative deconvolution approach. From the second derivative plot for each sample absorbance spectrum, peaks and local minima were identified and their numbers and positions were manually placed to deconvolute the absorbance spectra. Afterwards, the resulting area, amplitude and center values of the fitted bands were exported as a table and plotted.

2.6. Transmission Electron Microscopy (TEM)

The size and morphology of the Sup35-LCB1/3 self-assembled fibrils prepared under different salt concentration were examined using negative staining transmission electron microscopy (NS-TEM). All the samples were prepared by placing 10 μL of fibril suspensions (1:10 dilution) on carbon-coated copper grids. The excess of solution was removed after 10 min incubation with filter paper strips. The samples were then negatively stained with 10 μL of uranyl acetate solution (2 % w/v) for 1 min. The grids were imaged with a 120 kV JEOL 1400 transmission electron microscope (JEOL Ltd, Japan). Images of representative amyloid fibrils were acquired with a CCD GATAN ES1000W Erlangshen camera (Gatan Inc., USA). Fibrils width measurements were done in random positions of the grids using ImageJ software (National Institutes of Health, Bethesda, Maryland, USA). The obtained width average was a result of 30 individual measures for each sample. For group-wise comparisons, a two-way ANOVA test of the data was performed using GraphPad Prism V6.01 [49].

2.7. Sup35-LCB1/3 fibrils resistance to sodium dodecyl sulfate (SDS)

0.8 μg/μL of Sup35-LCB1 and Sup35-LCB3 fibrils, formed under three different Na-PB conditions, were taken after they had been separated from their soluble protein counterparts at the end of the fibrillation. These fibrils were then incubated in the absence and presence of 0.1 % and 1 % SDS for 30 min at 25 °C. After incubation, the samples were centrifuged at 16100 g for 45 min at 20 °C to separate the fibrillar remains from any dissociated or soluble component. Subsequently, 10 μL of the supernatants from both the control and treated samples were mixed with an equal volume of loading buffer. The mixture was then boiled for 10 min at 95 °C. Subsequently, 12 μL of each sample was loaded onto a 15 % SDS-PAGE gel for analysis.

2.8. Modelling of Sup35-LCB1 nanofibrils

Fibrils were built with a 2° left angle twist, maintaining a 4.8-angstrom translation over the Z-axis between the monomers. The LCB1 domain was extracted from the Cryo-EM structure of the mini-binder bound to the SARS-CoV-2 Spike protein (pdb entry 7JZU). However, due to the relatively low resolution of the structure (3.1 Å), the sidechains of some amino acids were not determined. Therefore, the structure was refined using the ColabFold Google notebook [50] and the original pdb as a structure template. The obtained structure contained all residues' sidechains, maintaining the structure of the original pdb. The functionalized fibril models were built from hexameric subunits of the LCB1 domain bound to the amyloid fibril through the linker. The subunit's architecture maintained equidistant and maximum spacing between the LCB1 domains and the core of the fibril. An imaginary circle around the fibrils' extreme was populated with the globular domains using sine and cosine theorems. Afterwards, the globular domains were connected to the fibril using the linker sequence, and the hexameric subunits were concatenated 15 times along the z axis to build the final fibril model, consisting of 90 monomers. Finally, the complete model was energy minimized and analyzed for steric clashes. The process of fibril building was carried out using instructions written in Python and imported into ChimeraX [51]. The linker sequences were modelled into the final structure using the loop modelling capabilities of the MODELLER suite [52]. Finally, the structure was energy-minimized using GROMACS (v. 2022.3) [53] with the AMBER99SB-ILDN [54] force field and analyzed with the PROCHECK package [55].

2.9. Cytotoxicity assay

The effect of the Sup35-LCB1 nanofibrils on the cell viability of HeLa cells was investigated by performing a resazurin-based assay using the PrestoBlue TM Cell Viability Reagent (Invitrogen) as described in other articles [56–58]. In brief, HeLa cells (American Type Culture Collection, ATCC) were cultured in Dulbecco's Modified Eagle Medium (DMEM, Gibco, Invitrogen, USA) supplemented with 10 % (v/v) fetal bovine serum in 5 % CO_2 atmosphere at 37 °C. HeLa cells were plated out in a 96-well plate at a density of 3.5×10^3 cells/well in 100 μL complete DMEM. A reference well containing only the culture media was maintained as a control condition. The plate was incubated at 37 °C in 5 %

CO_2 for 24 h to allow for cell growth and adhesion to the culture plates. Then, Sup35-LCB1 fibrils in different salt conditions, diluted to the appropriate final concentration in DMEM (20, 50, and 100 μg/mL), were added to cells and incubated for 72 h in triplicates. The control group received the same volume of sterile PBS pH 7.0 as vehicle control. After incubation, 10 μL of the PrestoBlue cell viability reagent (Invitrogen) was added to each well and the plate was further incubated for 30 min. Cell viability was determined by recording fluorescence emission at 615 nm, with an excitation wavelength at 531 nm using a Victor III Multilabel Plate Reader (Perkin Elmer). Statistical analysis of the data, specifically checking for minimal differences, was performed using GraphPad Prism V6.01 [49], and the results were determined to be not statistically significant.

2.10. Interference of the ACE2-RBD interaction

The ability of the self-assembled Sup35-LCB1 fibrils formed in different salt condition to inhibit spike RBD-ACE2 interaction was evaluated using the Lumit™ SARS-CoV-2 Spike RBD: hACE2 Immunoassay (Promega Biotech). This assay utilizes the principle of luminescence complementation between two nonfunctional fragments (LgBiT and SmBiT) of the reporter protein NanoBiT®, achieving a full-length functional reporter upon reconstitution. To perform the experiments, the Sup35-LCB1 amyloid fibrils were serially diluted and incubated with RBD-FC (Rabbit Fc) for 30 min prior to the addition of hACE2-FC (Mouse Fc) and Lumit Antibody Mix. After 1-hour incubation at RT, Lumit™ detection reagent was added, followed by incubation at RT for 30 min, according to the manufacturer instructions. NanoBiT® Luminescence was then recorded using a fluorescence microplate reader (Spark®, Tecan). The signal from the buffer alone was subtracted from all samples signal to discard the background signal contribution. As control conditions, reactions without the Sup35-LCB1 fibrils were also assayed. Then, all luminescence values were expressed as percentage (%) of the maximal ACE2-RBD protein–protein interaction (PPI) activity. The corresponding sample neutralization activity (%) was determined by subtracting the PPI activity from 100. The IC_{50} values were determined using GraphPad Prism V6.01 [49] and applying a non-linear regression (least squares) fitting method. The final values represent the mean of two independent experiments.

2.11. Interference of SARS-CoV-2 cell internalization

The capacity of the Sup35-LCB1 nanofibrils to capture SARS-CoV-2 and inhibit its entry into cells was evaluated by using a cell culture-based assay (Promega Biotech), which exploits split NanoLuc technology (LgBiT and HiBiT). This approach uses engineered SARS-CoV-2 virus-like particles (VLPs) containing a HiBiT protein, which can efficiently deliver this cargo into target cells expressing intracellular LgBiT. Upon successful viral entry, this process results in the emission of a luminescence due to the reconstitution of NanoLuc within the infected cells. Importantly, the genome-free nature of SARS-CoV-2 −VLPs eliminates the need for a biosafety level 3 (BSL3) facility. Moreover, the HiBiT technology provides the benefits of high sensitivity and convenience of a single-reagent-addition step to quantify membrane fusion and virus cell entry. Serial dilutions of the self-assembled Sup35-LCB1 amyloid fibrils prepared in different salt conditions were incubated with SARS-CoV-2 S(G614) HiBiT- pseudotype VLPs for 30 min at 37 °C, before adding to SARS-CoV-2 HEK293T (LgBiT) target cells. After 3 h of incubation at 37 °C, Nano-Glo® live cell reagent was added, and luminescence of the cells was measured after 15 min incubation at 37 °C. If the virus binds to the engineered nanofibers, it cannot interact with the ACE2 receptor and be internalized into the cell. This prevents the release of HiBiT in the cell cytoplasm and, thus, no luminescence is produced. The buffer alone was assayed to determine the basal luminescence signal. Then, by subtracting the baseline-corrected luminescence signal values from 100, the inhibition of SARS-CoV-2 HiBiT- pseudotype VLPs entry was calculated and expressed as a function of the maximal neutralization percentage. In order to calculate the IC_{50}, the acquired values were fitted to a non-linear regression curve using the least squares fitting equation from GraphPad Prism V6.01 [49].

2.12. Coating with Sup35-LCB1 nanofibrils

To demonstrate the coating capacities of the Sup35-LCB1 nanofibrils, we conducted a dot blot assay. In this assay we have deposited the fibrils following a pattern to depict our university logo by spotting dots with 4 μg from LCB1 fibrils onto the methanol activated polyvinylidene difluoride membrane (PDVF) (Immobilon-P transfer membranes, Merck Millipore, Germany). Then, non-specific sites were blocked by incubating the membrane in 5 % BSA in TBS-T (20 mM Tris-HCl, pH 7.4, 150 mM NaCl, and 1 % Tween-20) for 30 min at RT. Next, the membrane was incubated with RBD-YFP protein (0.54 ng/μL) dissolved in 0.1 % BSA/TBS-T (30 min, RT); this allowed the RBD-YFP to bind specifically to the coated nanofibrils on the membrane. Then, the membrane was thoroughly washed with TBS-T (3x 5 min) to remove any unbound or nonspecifically bound RBD-YFP. Thus, only RBD-YFP specifically bound to the fibrils remained on the membrane. Finally, the membrane was imaged using a ChemiDoc imaging system (Bio-Rad Laboratories).

3. Results and discussion

3.1. Design and structural characterization of soluble Sup35-LCB1 and Sup35-LCB3 proteins

Recently, the self-assembly properties of prion-like proteins have been harnessed for creating novel nanomaterials with fibrillar morphology and large surface-to-volume ratios [34,42,59–61]. These proteinaceous materials are typically customized by selecting an amyloidogenic domain that can spontaneously self-assemble into fibrils and integrating it with functional globular domains. This modular approach enables tailoring both the structural properties and biological activities of these nanomaterials.

In this study, we aimed to develop novel nanofibrils with a high density of SARS-CoV-2 binding moieties, creating a functional supramolecular scaffold with antiviral properties. We have previously demonstrated that the Sup35-SAC sequence (a 21-residue segment corresponding to residues 98–118 of Sup35 prion domain) spontaneously self-assembles into amyloid fibrils, while preserving the structural integrity and functionality of appended globular domains [62]. Here, Sup35-SAC was used as a scaffolding unit and fused to LCB1 and LCB3 domains, serving as SARS-CoV-2 binding modules (Fig. 1). A short and flexible linker (SGSGS) was used to bridge the Sup35-SAC unit and the globular LCB domains in the protein fusions. This 5-residue linker is expected to allow both Sup35-SAC self-assembly into amyloid fibrils and the proper folding of the LCB moieties.

Recombinant expression of the Sup35-LCB1/LCB3 fusion proteins in *E. coli* cells followed by metal ion affinity chromatography yielded 21 mg of purified Sup35-LCB1 and 48 mg of Sup35-LCB3 per liter of culture (**Figs. S1 and S2**). The secondary structure of the soluble Sup35-LCB1/LCB3 proteins was analyzed using far-UV circular dichroism (CD) spectroscopy. The resulting spectra (Fig. 1**C and D**) exhibited characteristic spectral minima at 209 nm and 222 nm, indicative of α-helical conformations. These spectral signatures aligned well with the calculated α-helical secondary structure contents for Sup35-LCB1 and Sup35-LCB3 monomeric proteins, which were estimated to be 49 % and 51 %, respectively, supporting the preservation of the native folded states of LCB domains within the fusion proteins.

3.2. Sup35-LCB1/LCB3 spontaneously self-assemble into functional amyloid-like structures

The soluble precursors of amyloidogenic proteins can be directed

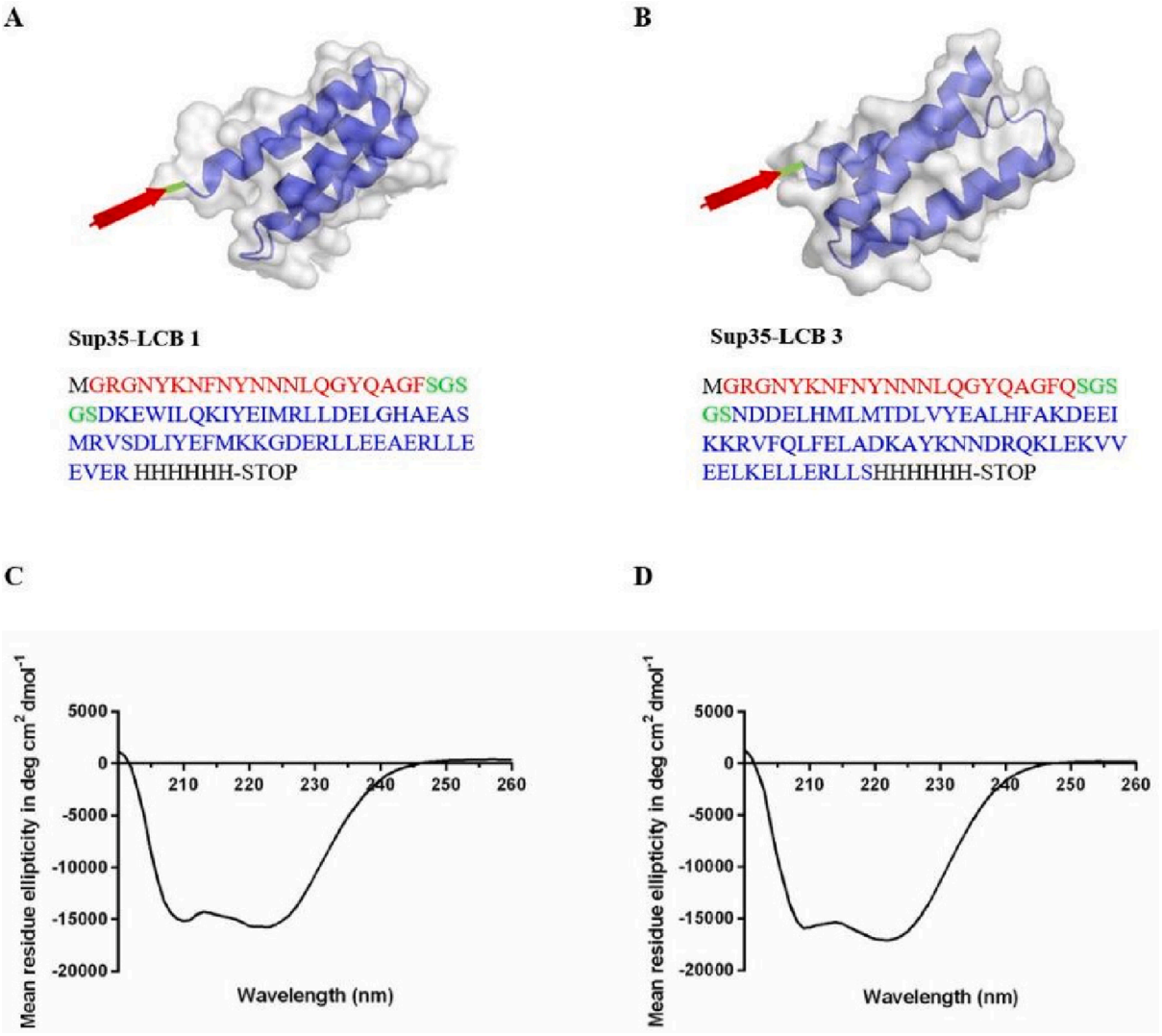

Fig. 1. Design and biophysical characterization of soluble Sup35-LCB1/LCB3 fusion proteins. (A, B) Cartoon representations and sequences of (A) Sup35-LCB1 and (B) Sup35-LCB3 fusion proteins. In these engineered proteins, the SAC of Sup35 (shown in red) is fused to either the LCB1 or LCB3 SARS-CoV-2 RBD binders (shown in blue) *via* a short S/G linker (shown in green). (C, D) Far-UV CD spectra of the purified (C) Sup35-LCB1 and (D) Sup35-LCB3 proteins recorded in the range of 200–260 nm at 25 °C in 20 mM sodium phosphate, pH 8.0, and at final protein concentration of 40 μM. (For interpretation of the references to colour in this figure legend, the reader is referred to the web version of this article.)

into distinct supramolecular structures by manipulating the assembly conditions [37,63–66]. Monomeric Sup35-LCB1/LCB3 proteins were incubated at an initial concentration of 500 μM for six days at 37 °C in varying concentrations of sodium phosphate (Na-PB) buffer at pH 8.0 (*i.e.,* 20 mM, 150 mM, and 300 mM). Unassembled monomers and prefibrillar species were removed from the reaction by centrifugation. Afterwards, protein concentrations in the insoluble fractions were estimated using the bicinchoninic acid (BCA) assay. Yields increased with increasing Na-PB concentration (**Table S1**). Fibrillation was most efficient at 300 mM Na-PB, with Sup35-LCB1 and Sup35-LCB3 yields of 58 % and 40 %, respectively, relative to the initial protein concentration in the reaction.

The amyloid-like nature of the purified protein aggregates was assessed by measuring their binding to thioflavin T (Th-T) and Congo red (CR) dyes (Fig. 2). At the same concentration, both Sup35-LCB1 and Sup35-LCB3 samples showed increased Th-T fluorescence in all assayed conditions. Notably, the Th-T fluorescence emission for the structures formed in 150 mM and 300 mM Na-PB exceeded that of those formed in 20 mM Na-PB. As expected, the soluble forms of Sup35-LCB1/LCB3 did not exhibit any Th-T binding (Fig. 2**A and B**). Similarly, the CR absorbance spectrum of the Sup35-LCB1/LCB3 aggregates displayed a clear red shift to approximately 540 nm, a characteristic feature associated with the binding of this dye to amyloid structures (Fig. 2**C and D**). This shift was consistently observed across all tested Na-PB conditions, becoming more pronounced at the highest salt concentrations.

These results collectively indicate the formation of amyloid fibrils in the Sup35-LCB1/LCB3 samples, particularly at higher salt concentrations. This suggests that charge screening may facilitate amyloid formation in these proteins. To further explore this hypothesis, we attempted to form amyloid fibrils in double-distilled Milli-Q™ water. Immediately after exchanging the buffer with water, the Sup35-LCB1/LCB3 protein solutions became cloudy and white, with a dramatic increase in the light scattering signal at 360 nm (**Fig. S3**). This indicates that protein precipitation occurs in the absence of counter ions, implying that a certain concentration of salt is necessary to sustain the solubility of the monomers and allow their slow, ordered assembly into amyloid structures.

We investigated the secondary structure content of Sup35-LCB1/LCB3 putative amyloid fibrils using attenuated total reflectance Fourier-transform infrared (ATR-FTIR) spectroscopy. The FTIR spectra

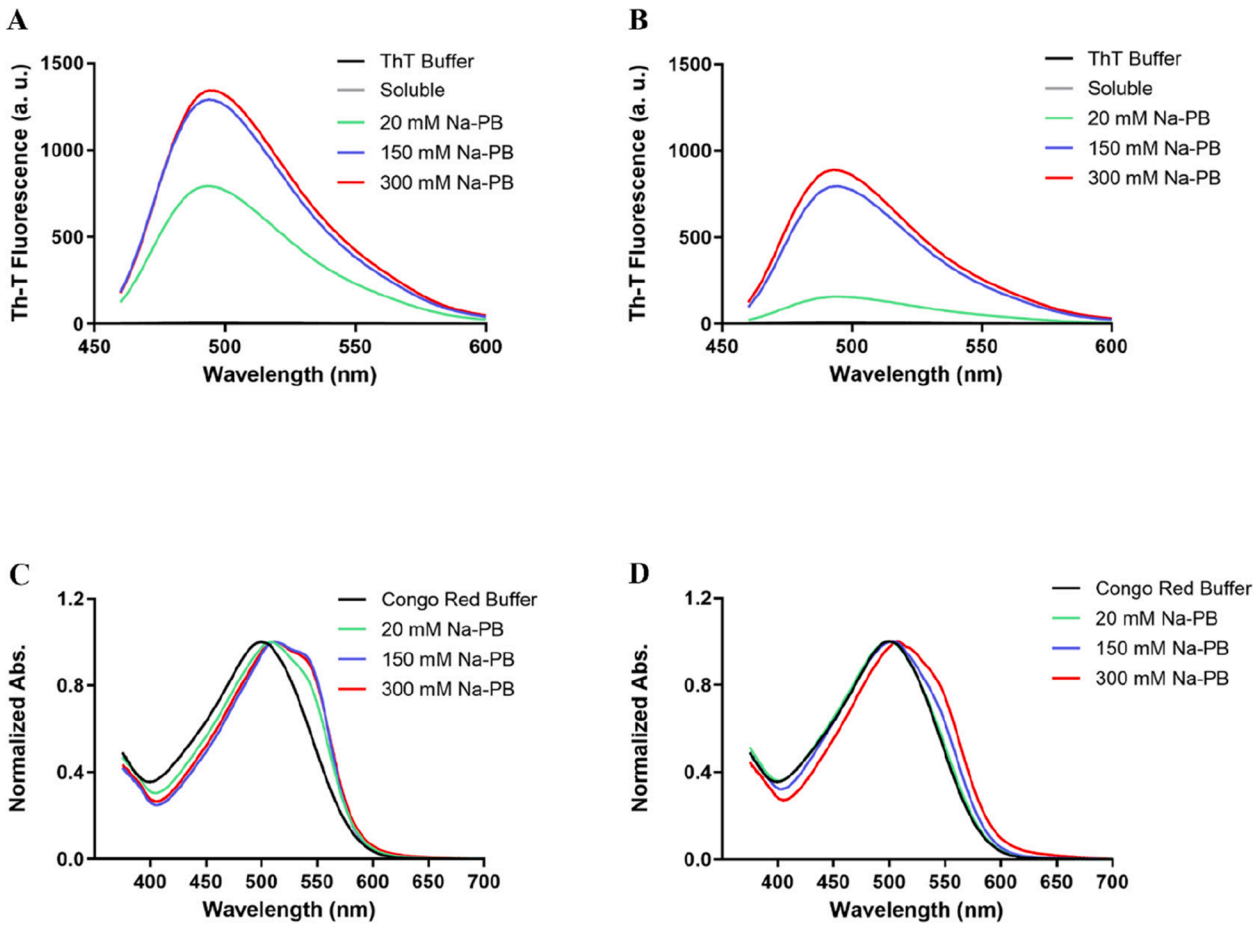

Fig. 2. Biophysical characterization of self-assembled Sup35-LCB1 and Sup35-LCB3. (A, B) Th-T fluorescence emission spectra in the presence of aggregated (A) Sup35-LCB1 and (B) Sup35-LCB3. Th-T fluorescence was recorded upon 445 nm excitation in the absence (black line) or in the presence of 0.2 mg/mL of the indicated protein samples. In (A, B), the Th-T signal of the buffer (ThT buffer) and the corresponding soluble monomeric proteins (Soluble) were evaluated as control conditions. (C, D) Congo Red (CR) normalized absorbance spectra in the absence (Congo Red Buffer) or in the presence of 0.2 mg/mL of aggregated (C) Sup35-LCB1 or (D) Sup35-LCB3. Note that CR absorbance spectra were recorded in the range from 375 to 700 nm. In figures A-D, the proteins were prepared and measured at three different Na-PB buffer concentrations, as follows: 20 mM (green solid line), 150 mM (blue solid line), and 300 mM (red solid line). (For interpretation of the references to colour in this figure legend, the reader is referred to the web version of this article.)

were recorded in the amide I region (1700 – 1600 cm^{-1}), which corresponds to the carbonyl absorption in the peptide bond. These absorbance spectra were then deconvoluted to determine the relative contributions of distinct secondary structure elements to the signal (Fig. 3). As outlined in **Table S2**, the fitted individual bands revealed three major shared contributions among the two types of assemblies at different Na-PB concentrations: ~34 % of the signal in 1626–1628 cm^{-1} range, a signature indicative of amyloid-like intermolecular β-sheets. A second major contribution occurs in the 1651/1652 cm^{-1} range, accounting for ~ 50 % of the spectra. This signal aligns well with the α-helix proportion previously detected by CD spectroscopy, suggesting the presence of properly folded LCB1/LCB3 globular domains. A third contribution, accounting for 10–20 % of the signal, is observed in the 1673–1675 cm^{-1} range, possibly arising from β-turns or random coil structures.

We monitored the secondary structure changes occurring in solution over time for both Sup35-LCB1 and Sup35-LCB3, incubated in 20 mM, 150 mM, and 300 mM Na-PB, recording the far-UV CD spectra at 0, 3, and 6 days (Fig. S4**A**). The presence of fibrils on day 6 was confirmed by microscopy (Fig. S4B).

The CD spectra of the initially soluble proteins (day 0) show two minima at 209 nm and 222 nm, indicating a predominant α-helix structure, likely contributed by the highly helical LCB1/3 domains. Interestingly, and consistent with the FTIR data, the results suggest that the globular domains remain in a helical conformation in the fraction of protein transitioning to fibrils, as the spectra of the different solutions did not exhibit major shifts toward a β-sheet-rich structure during the fibrillation reaction (Fig. S4A). The incubation of Sup35-LCB1 in 300 mM Na-PB, and of Sup35-LCB3 at 150 and 300 mM Na-PB, results in a decrease in the overall CD signal, indicating that the fibrils tend to precipitate out of the solution. However, only in the case of Sup35-LCB3 is this change in intensity accompanied by a significant decrease of the 209 nm/222 nm intensity ratio, with a reduction of 13 % and 20 % in 150 and 300 mM Na-PB, respectively (Fig. S4A). These changes likely arise from the gain of certain β-sheet structure upon incubation.

Few examples of amyloids displaying cross-α structure have been reported [67,68] These instances involved the self-assembly of amphipathic α-helical peptides with antimicrobial activity. These peptides do not share sequential or structural similarity to the short Sup35 segment we use to build up the amyloid zipper of our fibrils. Indeed, we previously demonstrated that a peptide corresponding to this region is disordered in solution and transitions to an amyloid β-sheet structure [69].

Overall, our findings suggest that, under most conditions, an amyloid-like core and properly folded LCB moieties likely coexist within self-assembled Sup35-LCB1/LCB3.

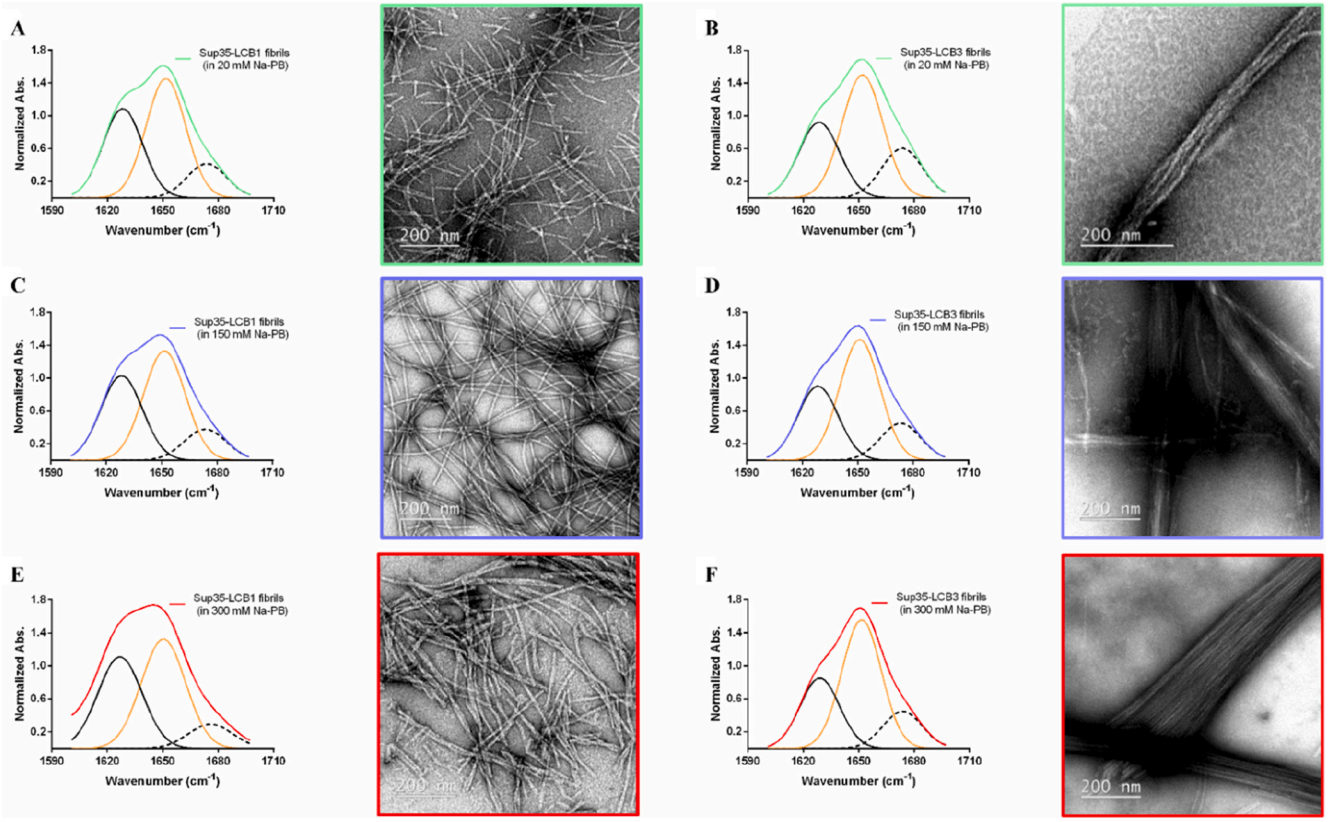

Fig. 3. Structural characterization of Sup35-LCB1 and Sup35-LCB3 self-assembled fibrils. (A-F) In the left panels, the second-derivative ATR-FTIR absorbance spectra in the amide I region are deconvoluted for: (A) Sup35-LCB1 and (B) Sup35-LCB3 fibrils formed in 20 mM Na-PB (depicted in green); (C) Sup35-LCB1 and (D) Sup35-LCB3 fibrils formed in 150 mM Na-PB (depicted in blue); (E) Sup35-LCB1 and (F) Sup35-LCB3 fibrils formed in 300 mM Na-PB (depicted in red). In each case, the fitted individual bands are indicated. The amyloid-like intermolecular β-sheet and α-helical components are shown as black and orange solid lines, respectively. In (A-F), right panels feature representative Negative-Stain Transmission Electron Microscopy (NS-TEM) images of the corresponding Sup35-LCB1/LCB3 amyloid assemblies, placed next to their respective FTIR plots. In all images, scale bar size is 200 nm. (For interpretation of the references to colour in this figure legend, the reader is referred to the web version of this article.)

3.3. Sup35-LCB1 and Sup35-LCB3 form different fibril polymorphs

It is now well-established that naturally occurring amyloid fibrils are generally polymorphic [37,64–66]. We have shown that the ionic strength of the solution not only influences the yield of Sup35-LCB1/LCB3 aggregates, but also shapes their biophysical properties. To further investigate the macromolecular organization of these insoluble structures, we used Negative-Stain Transmission Electron Microscopy (NS-TEM) (Fig. 3). Sup35-LCB1 assembled at the lowest salt concentration (*i.e.,* 20 mM Na-PB) displayed isolated, straight, unbranched, and uniform fibrils (Fig. 3**A**), with an average diameter of 10.8 ± 1.3 nm (**Fig. S5**). In contrast, at 150 mM and 300 mM Na-PB, the amyloid fibrils appeared much longer and exhibited a twisted morphology (Fig. 3**C and E**), with characteristic diameters of 12.3 ± 2.1 nm and 17.4 ± 4.2 nm, respectively (**Fig. S5**). Notably, the architecture of these amyloid scaffolds persisted even after one month of incubation at RT, suggesting that these structures are indeed stable polymorphic species (**Fig. S6**). While we cannot entirely rule out the presence of mixed fibril conformers in the samples, their uniform morphology under each specific salt condition suggests that this is not a predominant feature of Sup35-LCB1 fibril preparations.

To our surprise, TEM images of Sup35-LCB3 fibrils revealed a distinct morphology, characterized by laterally associated fibrils that coalesced into dense stacks of highly elongated structures tightly clustered together, resulting in significantly larger diameters, ranging from 70 to 190 nm (Fig. 3**B, D and F**). This behavior was particularly pronounced at higher salt concentrations. Intrigued by this discrepancy in spatial organization, we delved into the possibility that distinct stickiness properties of LCB1 and LCB3 might be at play, since regions prone to aggregation (APRs) on protein surfaces are often involved in intermolecular interactions [70–73].

We analyzed LCB1 and LCB3 domains using Aggrescan 3D 2.0 [74]. For the calculations, we utilized the X-ray crystal structures of LCB1 (PDB: 7JZU) and LCB3 (PDB: 7JZM) domains [45]. Our findings revealed that LCB3 has a lower net charge and higher surface aggregation propensity compared to LCB1, being thus more sticky (**Fig. S7**), a property that likely contributes to the tendency of filaments adorned with LCB3 to form lateral associations.

Fibril stability is often approached by evaluating the resistance to disassembly in the presence of SDS [75]. To investigate their stability, Sup35-LCB1 and Sup35-LCB3 fibrils formed under different Na-PB conditions were collected and incubated in the absence of SDS or in the presence of 0.1 % and 1 % SDS. The samples were then centrifuged, and the levels of fibril-dissociated soluble protein in the supernatant were analyzed by SDS-PAGE (**Fig. S8**).

The results revealed that Sup35-LCB3 fibrils are sensitive to both 0.1 % and 1.0 % SDS concentrations across all salt conditions. In contrast, the Sup35-LCB1 fibrils show significant resistance to SDS when formed in 300 and 150 mM Na-PB, but not at 20 mM Na-PB. These findings suggest that the interplay between sequence and solution conditions modulates fibril conformation and stability.

In light of these results, we decided to focus our subsequent experiments exclusively on the individual fibrils formed by Sup35-LCB1 since Sup35-LCB3 were generally less stable, and their lateral association might hinder SARS-CoV-2 spike protein access to the LCB3 binding site.

3.4. Molecular architecture of Sup35-LCB1 amyloid fibrils

Amyloid fibril-based materials are well-defined supramolecular assemblies with mesoscopic dimensions, often displaying elongated helicoidal dispositions [42,76]. We generated a molecular model of the Sup35-LCB1 nanofibril to inspect its general architecture and confirm the feasibility of forming a helical amyloid core with protruding LCB1 domains without steric hindrance (Fig. 4). For the parallel and in-register cross-β amyloid core, we used two structural arrangements: stacks of linear β-strands and of β-arches, both displaying a left-handed twist with an axial twist angle of 2° per 4.8 Å step [42]. The globular domains were evenly distributed, maintaining a distance of 25 Å from the central axis of rotation. These initial rigid models provided adequate separation between LCB1 domains, preventing their main chains from overlapping or intertwining. The two generated structural models comprised 90 monomers, contributing to a total helix turn of 180°. Each monomer advanced 4.9 Å, with a total displacement of 29.5 Å for a hexamer. Subsequently, we employed MODELLER [52] to incorporate the linker sequence that connected each core fibril monomer to the correspondent LCB1 domain. These models underwent energy minimization using the steepest descent algorithm of GROMACS [53] with the AMBER99SB-ILDN [54] force field, to minimize repulsive forces arising from close contacts between side chains.

Our molecular modeling analysis validated that parallel and in-register cross-β amyloid fibers allow for the accommodation of LCB1 globular domains (Fig. 4**).** We evaluated the resulting structure using the PROCHECK package [55], confirming the absence of steric clashes among the domains of the built models. These models had a diameter of 8.2 nm for the fibrils forming β-arches and 11.8 nm for the linear β-strands, compatible with the sizes we identified experimentally. However, the predominance of the α-helix signal relative to the β-sheet one in the CD spectra is in favor of the β-arches fibril mode, where the globular domain nearly fully envelops the inner amyloid zipper, shielding it from the solvent and consequently from the incoming polarized light in CD experiments.

3.5. Biocompatibility of Sup35-LCB1 amyloid nanofibrils

Sup35-LCB1 nanofibrils hold potential for material applications. However, the surfaces of amyloids can be potentially cytotoxic [78–80]. To rule out this possibility, we evaluated the cytotoxic effects of Sup35-LCB1 nanofibrils on human cells using the Prestoblue® cell viability reagent. HeLa cells were exposed to increasing concentrations of Sup35-LCB1 nanofibrils, prepared at 20, 150 or 300 mM Na-PB, and cell viability was assessed after 72 h of incubation (Fig. 5).

Notably, treatment with these synthetic amyloid fibrils did not induce any significant reduction in cell viability, even at the highest concentration of 100 μg/mL. This result underscores the non-cytotoxic nature of the various Sup35-LCB1 assemblies, indicating their suitability for developing biocompatible nanomaterials.

3.6. Sup35-LCB1 nanofibrils disrupt Spike RBD-ACE2 interaction

The interaction between the RBD of SARS-CoV-2 Spike protein and the ACE2 receptor was assessed using a Lumit immunoassay. This assay relies on the detection of the interaction between Rabbit Fc-tagged SARS-CoV-2 RBD (rFc-RBD) and Mouse Fc-tagged human ACE2 (mFc-ACE2). It employs secondary antibodies labelled with the NanoLuc luciferase LgBit and SmBit subunits. When these antibodies bind to their respective epitopes, the LgBit and SmBit fragments come into close proximity, enabling the reconstitution of an active luciferase enzyme. This enzyme subsequently emits bioluminescence, the intensity of which is directly proportional to the strength of the RBD-ACE2 interaction. Consequently, if the RBD-ACE2 interaction is hindered or blocked, the LgBit and SmBit fragments will not come together, resulting in a decreased bioluminescent signal (Fig. 6**A**). This method not only provides a quantitative measure of the RBD-ACE2 interaction but also offers a sensitive approach to screen potential inhibitors of this critical viral-host interaction, which is essential for SARS-CoV-2 infection.

We investigated the ability of Sup35-LCB1 nanofibrils to interfere with the RBD-ACE2 interaction. First, we measured the inhibitory activity of freshly prepared nanofibrils using the Lumit assay (Fig. 6**B**). These amyloid fibrils demonstrated a remarkable ability to thwart the RBD-ACE2 interaction. The inhibitory potency varied depending on the

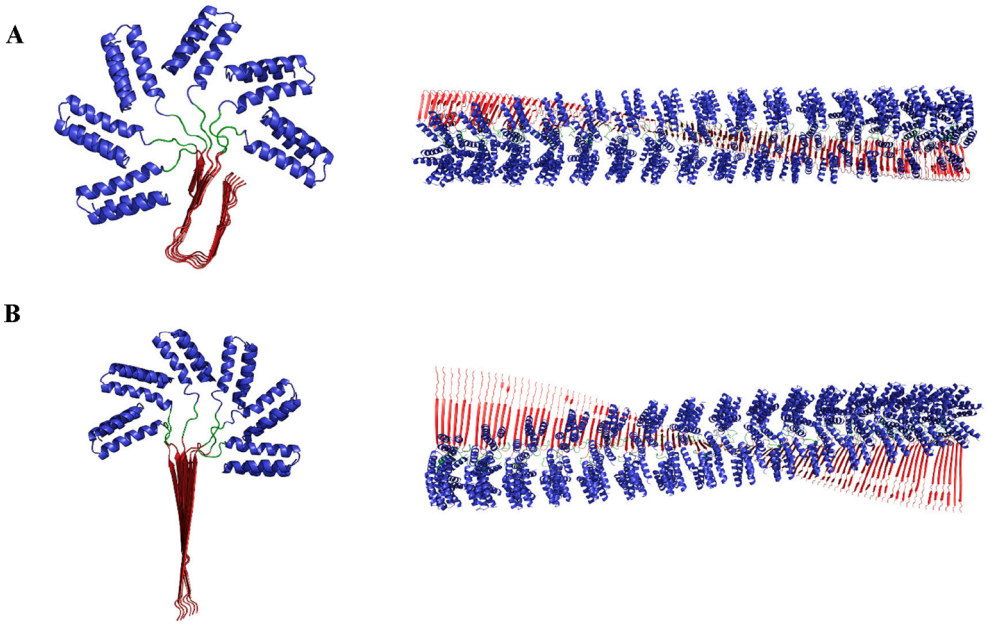

Fig. 4. Structural models of amyloid fibrils formed by the self-assembly of Sup35-LCB1 monomers. (A) Fibril formation through stacked β-arches and (B) linear β-strands. The Sup35 SAC domain, the linker, and the LCB1 domains are colored in red, green, and blue, respectively. In (A, B), left panels show the axial representation of a single fiber hexamer. The right panels display the lateral representation of the 90-monomers fibril. All representations were done using the PyMol software [77]. (For interpretation of the references to colour in this figure legend, the reader is referred to the web version of this article.)

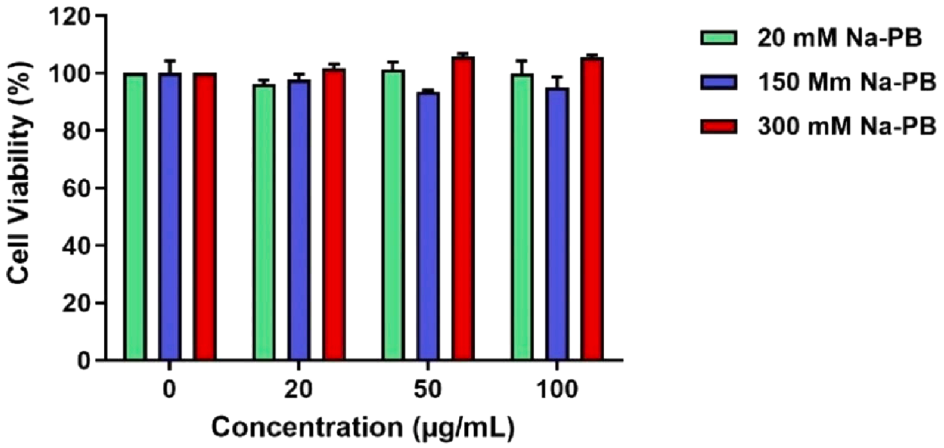

Fig. 5. Cytotoxicity of Sup35-LCB1 self-assembled nanofibrils. Cell viability of HeLa cells after 72 h of incubation in the presence of different concentrations of Sup35-LCB1 nanofibrils. Results are shown as mean ± SD (n = 3).

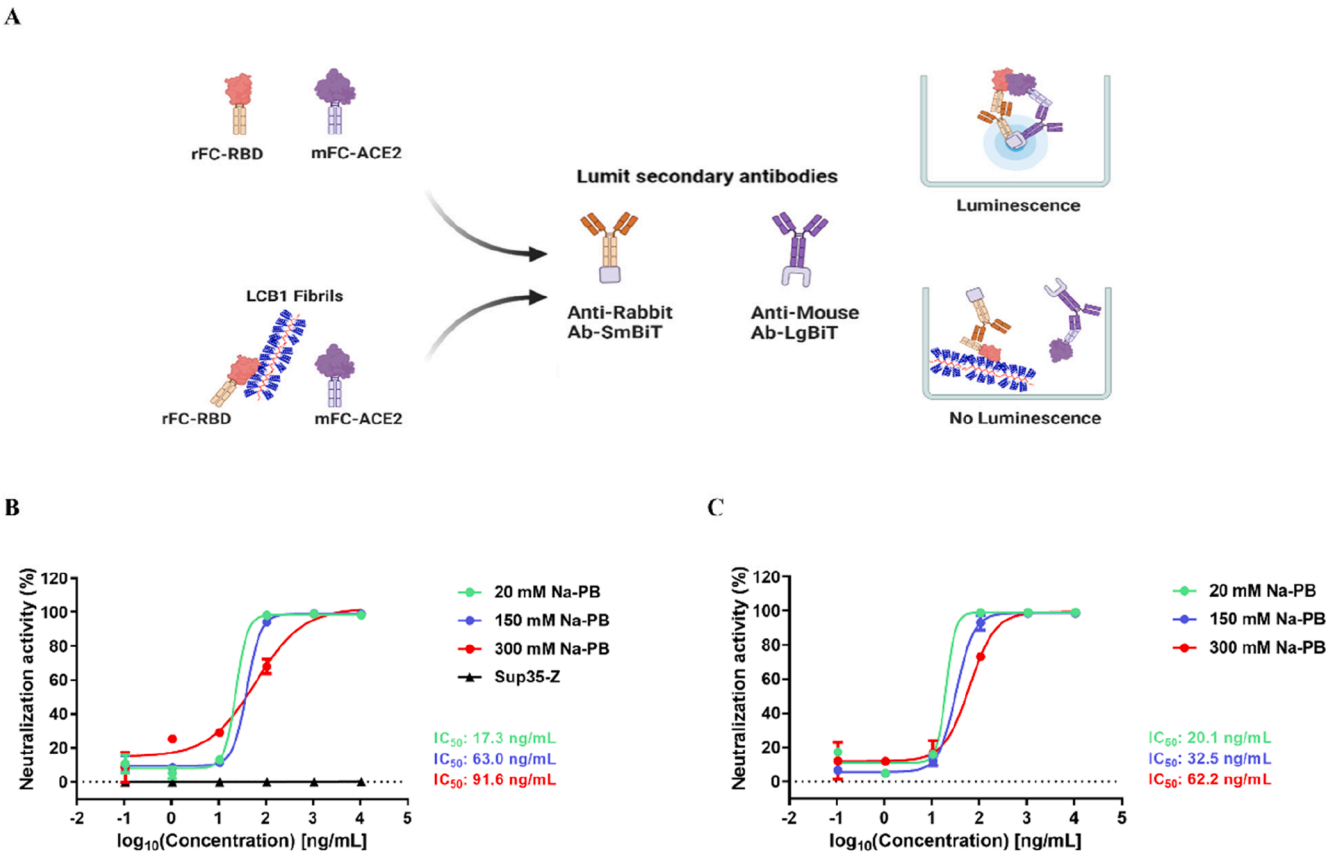

Fig. 6. Inhibition of the RBD-ACE2 interaction by Sup35-LCB1 self-assembled nanofibrils. (A) Schematic representation of the Lumit™ SARS-CoV-2 Spike RBD-ACE2 Immunoassay. Created using BioRender (BioRender.com). (B, C) The RBD-ACE2 interaction is inhibited by self-assembled Sup35-LCB1 nanofibrils. The inhibitory effect against the interaction between the RBD and ACE2 was evaluated using (B) freshly prepared nanofibrils, which includes amyloid fibrils of Sup35 SAC fused to a Z-domain (Sup35-Z) as a control condition, Additionally, (C) represents the nanofibrils after 1-month incubation at room temperature (RT). Note that the assayed Sup35-LCB1 nanofibrils were prepared under different Na-PB concentrations (*i.e.*, 20, 150, and 300 mM Na-PB). Data is presented as mean ± SD (n = 2). IC_{50} values were calculated by fitting the data to a non-linear regression (least squares) equation using GraphPad software [49].

Na-PB concentration used during fibril formation. Specifically, the IC_{50} values were determined to be 17.3 ng/mL for fibrils formed in 20 mM Na-PB, 63.0 ng/mL for those in 150 mM Na-PB, and 91.6 ng/mL for fibrils in 300 mM Na-PB (Fig. 6**B**). To assess the specificity of binding, we included fibrils formed by Sup35-SAC fused to the Z-domain (Sup35-Z) as a negative control. The Z-domain is an engineered protein analog of the B domain of *Staphylococcus aureus* protein A, which was selected for its similar size (approximately 6.5 kDa) and α-helical fold to the LCB1 domain [44] (**Fig. S9**). This comparative analysis confirmed the specific inhibitory effect of Sup35-LCB1 nanofibrils on the RBD-ACE2 interaction.

In a second Lumit experiment, we evaluated the same amyloid fibrils after one month of incubation at room RT (Fig. 6**C**). The results confirmed that the nanostructures' SARS-CoV-2 binding activity was

preserved, proving that Sup35-LCB1 nanofibrils are durable and reliable functional materials.

3.7. SARS-CoV-2 trapping and neutralization using Sup35-LCB1 nanofibrils

To evaluate the efficacy of Sup35-LCB1 nanofibrils in capturing and neutralizing SARS-CoV-2, we investigated their ability to impede viral entry into mammalian cells. To circumvent the risks associated with handling live viruses, we employed a SARS-CoV-2 HiBiT- pseudotype VLP assay, based on Promega Biotech's NanoBiT® technology (Fig. 7**A**). This bioassay utilizes a bioluminescent reporter cell-based approach and is routinely used to evaluate the neutralization capacity of ligands and antibodies that specifically target SARS-CoV-2 entry into the host cells [23].

In this assay, pseudotyped HiBiT-tagged virus-like particles (VLPs) bearing the trimeric SARS-CoV-2 Spike protein were pre-incubated with increasing concentrations of Sup35-LCB1 nanofibrils (ranging from 0.1 to 10,000 ng/mL) formed at 20, 150, and 300 mM Na-PB concentrations. After incubation with the nanofibrils, they were added to the hACE2-HEK293T (LgBiT) target cells, allowing for the determination of the neutralizing activity of these nanomaterials (Fig. 7**B**). The calculated IC_{50} values for the neutralizing activity of Sup35-LCB1 nanofibrils were determined to be 5.6 ng/mL, 22.4 ng/mL, and 34.1 ng/mL for the samples produced at 20 mM, 150 mM, and 300 mM Na-PB concentrations, respectively. The ranking of neutralization activities is consistent with this of the binding results obtained in the Lumit assay, supporting the specific activity of these fibrillar structures against the RBD-ACE2 interaction. The 3-fold higher potencies displayed in this assay likely stem from an avidity effect, where three LCB1 domains can simultaneously bind to the trimeric Spike protein.

The results indicate a dose-dependent neutralization effect and demonstrate a high potency of Sup35-LCB1 nanofibrils in preventing the fusion of pseudotyped SARS-CoV-2 VLPs with the membrane of human ACE2-expressing cells. Importantly, they display lower neutralization IC_{50} values than those reported for therapeutic antibodies like bamlanivimab, imdevimab, and etesevimab tested in the same assay (Table 1).

Taken together, our data unequivocally demonstrate that Sup35-LCB1 nanofibrils constitute a functional nanostructure capable of capturing and neutralizing SARS-CoV-2 viruses through selective interactions with RBD of the spike protein. This immediately suggests their potential applicability in creating novel functional surface coatings with selective antiviral properties.

3.8. Surface coating with functional Sup35-LCB1 nanofibrils

Recent reports demonstrated that surface contact can spread SARS-CoV-2, thus contributing to its rapid transmission [82], with wet surfaces being associated with longer virus survival times [83]. Consequently, eradicating surface transmission, particularly on wet surfaces, is essential in curbing the spread of COVID-19. This entails developing novel materials with intrinsic antiviral properties. In this regard, the ability of fibrils to form densely packed networks and solid thin films, facilitates their selective application and deposition onto specific areas of a given surface substrate. As proof-of-concept, we applied Sup35-LCB1 nanofibrils onto a polyvinylidene difluoride (PVDF) membrane (Fig. 8**A**). Our objective was crafting our university logo by immobilizing the fibrils onto the PVDF matrix. To gauge the functionality of this patterned surface, we evaluated its capacity to bind a fluorescent YFP-conjugated version of the spike protein RBD domain (YFP-RBD) [84]. This provides a means for rapidly visualizing the nanofibril/RBD interaction at the PVDF surface using a standard Fluorescence Imaging System.

Table 1
SARS-CoV-2 HiBiT- pseudotype VLP assay response to neutralizing antibodies and Sup35-LCB1 nanofibrils.

SARS-CoV-2 Spike Neutralizing mAb / material	IC_{50} (ng/mL)
Bamlanivimab	34.0*
Imdevimab	72.0*
Etesevimab	230.0*
LCB1 Fibrils (20 mM Na-PB)	5.6
LCB1 Fibrils (150 mM Na-PB)	22.4
LCB1 Fibrils (300 mM Na-PB)	34.1

* Experimental data provided by Promega Biotech Ibérica, S.L.

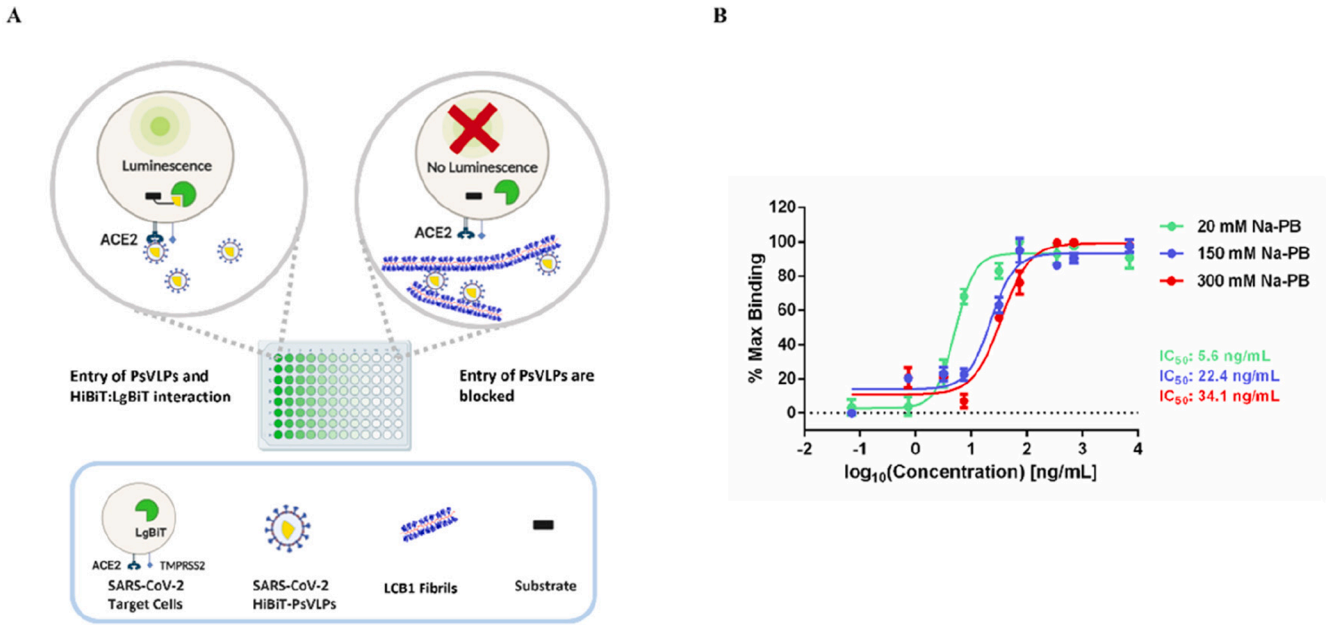

Fig. 7. SARS-CoV-2 trapping and neutralization effect of Sup35-LCB1 self-assembled nanofibrils. (A) Schematic representation of the SARS-CoV-2 HiBiT- pseudotype VLPs assay that uses Promega Biotech's NanoBiT® technology [23,81]. Created using BioRender (BioRender.com). (B) Detection of cell entry of pseudotyped VLPs into the SARS-CoV-2 HEK 293 T target cells containing the LgBiT protein reporter. Data represents the percentage of neutralization (%), and values are presented as mean ± SD (n = 2). IC_{50} values were calculated by fitting the experimental data to a non-linear regression (least squares) equation using GraphPad software [49].

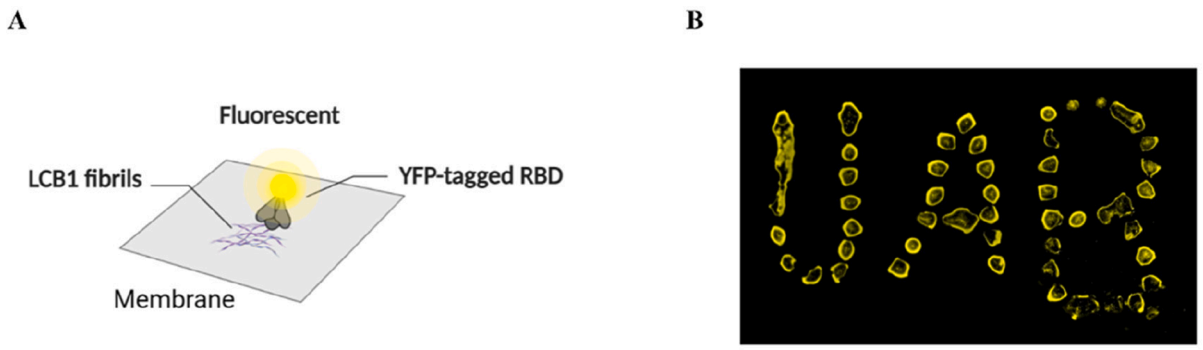

Fig. 8. Surface coating of PVDF membranes using Sup35-LCB1 nanofibrils. (A) Schematic representation of the PVDF surface decoration with Sup35-LCB1 amyloid nanofibrils and their subsequent binding to the fluorescently labeled YFP-RBD protein in the aqueous phase. (B) YFP fluorescence image of the printed PVDF surface, demonstrating the specific binding of the YFP-RBD to the nanofibril-coated areas.

As depicted in Fig. 8**B**, the resulting fluorescence image clearly conveys the intended logo, showcasing the successful printing of fibrils onto the PVDF matrix and the efficient binding of the YFP-RBD to the nanofibril-coated surface. This application of Sup35-LCB1 nanofibrils illustrates the potential of our modular strategy in creating functionalized surfaces which can be customized to meet specific requirements, including antiviral applications.

4. Conclusion

The COVID-19 pandemic has posed unprecedented challenges to global health, prompting the accelerated development of novel therapeutics, exemplified by mRNA vaccines, which have substantially mitigated the risk of severe illness, hospitalization, and death. However, vaccination does not guarantee complete protection against infection. Vaccinated individuals can still contract SARS-CoV-2 and transmit the virus to others primarily through aerosols, droplets, or contaminated surfaces [10–12]. As a result, the development of materials and surface coatings with SARS-CoV-2 antiviral properties has garnered increasing attention [27,85]. However, most of the reported approaches still rely on toxic substances that lack virus specificity [28,30,31].

Drawing inspiration from the modular nature of yeast prions, we have genetically engineered a novel fibrillar biomaterial that leverages the Sup35-SAC domain as a scaffold and the high-affinity SARS-CoV-2 of LCB1/LCB3 binders as functional domains. This fusion technology enables efficient protein production at high yields, making it cost-effective and scalable. The self-assembly of these polypeptides into amyloid-like nanofibrils occurs spontaneously and the structural and functional properties of the final assemblies can be controlled by modulating the ionic strength of the solution.

In particular, Sup35-LCB1 assembles into discreet, regular, non-toxic amyloid-like structures, forming interwoven fibrillar networks. These biocompatible nanofibrils exhibit a high aspect ratio, displaying the LCB1 binding motif in its folded and functional form at a high density on their surfaces, which confers remarkable avidity. This proves instrumental in effectively inhibiting the interaction between the SARS-CoV-2 Spike RBD and the ACE2 receptor, a critical step in viral entry into host cells. Accordingly, our engineered nanofibrils demonstrated potent SARS-CoV-2 neutralizing activity in a cellular model of infection, with neutralization IC_{50} values as low as 5.6 ng/mL, surpassing the performance of existing therapeutic antibodies in the same assay.

Furthermore, we successfully imprinted these nanofibrils onto a PVDF membrane, creating functionalized surfaces capable of capturing the SARS-CoV-2 Spike in wet environments. This exemplifies the potential of the nanofibrils to serve as a safe functional surface coating materials to contain viral spread and increase safety of personal protective equipment. Additionally, the polymer fibrils could potentially replace antibodies in existing tests at a lower cost. They may also find utility in concentrating and isolating viral particles for individual testing or environmental sampling. Importantly, due to the modularity of our strategy, replacing the LCB1 moiety with alternative virus binders would allow tailoring the viral specificity of the nanostructure.

In conclusion, the Sup35-LCB1 amyloid-based nanofibrils represent a promising functional material in the fight against COVID-19 and other viral pandemics, offering potential prophylactic and diagnostic applications.

CRediT authorship contribution statement

Molood BehBahanipour: Writing – review & editing, Writing – original draft, Visualization, Methodology, Investigation, Funding acquisition, Formal analysis. **Susanna Navarro:** Writing – original draft, Validation, Supervision, Methodology. **Oriol Bárcenas:** Writing – review & editing, Visualization, Software, Methodology, Funding acquisition, Formal analysis. **Javier Garcia-Pardo:** Writing – review & editing, Validation, Funding acquisition. **Salvador Ventura:** Writing – review & editing, Validation, Supervision, Resources, Project administration, Funding acquisition, Conceptualization.

Declaration of competing interest

The authors declare that they have no known competing financial interests or personal relationships that could have appeared to influence the work reported in this paper.

Data availability

Data will be made available on request.

Acknowledgements

This work was funded by the Spanish Ministry of Science and Innovation (MICINN, Spain) PID2022-137963OB-I00 to S.V.; By ICREA, (ICREA-Academia 2020, Spain) and by EU (PhasAge H2020-WIDESPREAD-2020-5, EU) to S.V. J.G.-P. was supported by the Spanish Ministry of Science and Innovation with a Juan de la Cierva Incorporacion (IJC2019-041039-I, Spain) M.B. was supported by the Spanish Ministry of Science and Innovation (PRE2020-092634, Spain). This article is partially based upon work from COST Action ML4NGP, CA21160, supported by COST (European Cooperation in Science and Technology, European Union). O. B. was supported by the Spanish Ministry of Science and Innovation via a doctoral grant (FPU22/03656, Spain). We thank Dr. Roger M Benoit for gently providing us with the RBD-YFP protein.

Appendix A. Supplementary data

Supplementary data to this article can be found online at https://doi.org/10.1016/j.jcis.2024.06.175.

References

[1] Z.-R. Yang, Y.-W. Jiang, F.-X. Li, D. Liu, T.-F. Lin, Z.-Y. Zhao, et al., Efficacy of SARS-CoV-2 vaccines and the dose–response relationship with three major antibodies: a systematic review and meta-analysis of randomised controlled trials, The Lancet Microbe. (2023), https://doi.org/10.1016/S2666-5247(22)00390-1.

[2] L. Riva, S. Yuan, X. Yin, L. Martin-Sancho, N. Matsunaga, L. Pache, et al., Discovery of SARS-CoV-2 antiviral drugs through large-scale compound repurposing, Nature 586 (2020) 113–119, https://doi.org/10.1038/s41586-020-2577-1.

[3] D.E. Gordon, G.M. Jang, M. Bouhaddou, J. Xu, K. Obernier, K.M. White, et al., A SARS-CoV-2 protein interaction map reveals targets for drug repurposing, Nature 583 (2020) 459–468, https://doi.org/10.1038/s41586-020-2286-9.

[4] M.J. Joyner, R.E. Carter, J.W. Senefeld, S.A. Klassen, J.R. Mills, P.W. Johnson, et al., Convalescent plasma antibody levels and the risk of death from covid-19, N Engl. J. Med. 384 (2021) 1015–1027, https://doi.org/10.1056/NEJMoa2031893.

[5] R. Libster, G. Perez Marc, D. Wappner, S. Coviello, A. Bianchi, V. Braem, et al., Early high-titer plasma therapy to prevent severe covid-19 in older adults, N Engl. J. Med. 384 (2021) 610–618, https://doi.org/10.1056/NEJMoa2033700.

[6] N.A.J. McMillan, K.V. Morris, A. Idris, RNAi to treat SARS-CoV-2-variant proofing the next generation of therapies, EMBO Mol. Med. 14 (2022) e15811, https://doi.org/10.15252/emmm.202215811.

[7] B. Berber, C. Aydin, F. Kocabas, G. Guney-Esken, K. Yilancioglu, M. Karadag-Alpaslan, et al., Gene editing and RNAi approaches for COVID-19 diagnostics and therapeutics, Gene Ther. 28 (2021) 290–305, https://doi.org/10.1038/s41434-020-00209-7.

[8] Z. Tang, N. Kong, X. Zhang, Y. Liu, P. Hu, S. Mou, et al., A materials-science perspective on tackling COVID-19, Nat. Rev. Mater. 5 (2020) 847–860, https://doi.org/10.1038/s41578-020-00247-y.

[9] B. Wichmann, R. Moreira Wichmann, Big data evidence of the impact of COVID-19 hospitalizations on mortality rates of non-COVID-19 critically ill patients, Sci. Rep. 13 (2023) 13613, https://doi.org/10.1038/s41598-023-40727-z.

[10] Y. Bai, L. Yao, T. Wei, F. Tian, D.Y. Jin, L. Chen, M. Wang, Presumed asymptomatic carrier transmission of COVID-19, JAMA 323 (2020) 1406–1407, https://doi.org/10.1001/jama.2020.2565.

[11] N. van Doremalen, T. Bushmaker, D.H. Morris, M.G. Holbrook, A. Gamble, B. N. Williamson, et al., Aerosol and surface stability of SARS-CoV-2 as compared with SARS-CoV-1, N Engl. J. Med. 382 (2020) 1564–1567, https://doi.org/10.1056/NEJMc2004973.

[12] S.Y. Ren, W.B. Wang, Y.G. Hao, H.R. Zhang, Z.C. Wang, Y.L. Chen, R.D. Gao, Stability and infectivity of coronaviruses in inanimate environments, World J. Clin. Cases. 8 (2020) 1391–1399, https://doi.org/10.12998/wjcc.v8.i8.1391.

[13] M. Letko, A. Marzi, V. Munster, Functional assessment of cell entry and receptor usage for SARS-CoV-2 and other lineage B betacoronaviruses, Nat. Microbiol. 5 (2020) 562–569, https://doi.org/10.1038/s41564-020-0688-y.

[14] M. Hoffmann, H. Kleine-Weber, S. Schroeder, N. Kruger, T. Herrler, S. Erichsen, et al., SARS-CoV-2 cell entry depends on ACE2 and TMPRSS2 and is blocked by a clinically proven protease inhibitor, Cell 181 (2020) 271–280 e278, https://doi.org/10.1016/j.cell.2020.02.052.

[15] F. Liu, X. Long, B. Zhang, W. Zhang, X. Chen, Z. Zhang, ACE2 expression in pancreas may cause pancreatic damage after SARS-CoV-2 infection, Clin. Gastroenterol. Hepatol. 18 (2020) 2128–2130 e2122, https://doi.org/10.1016/j.cgh.2020.04.040.

[16] K. Nepali, R. Sharma, S. Sharma, A. Thakur, J.P. Liou, Beyond the vaccines: a glance at the small molecule and peptide-based anti-COVID19 arsenal, J. Biomed. Sci. 29 (2022) 65, https://doi.org/10.1186/s12929-022-00847-6.

[17] S.K. Nayak, Inhibition of S-protein RBD and hACE2 interaction for control of SARSCoV- 2 infection (COVID-19), Mini Rev. Med. Chem. 21 (2021) 689–703, https://doi.org/10.2174/1389557520666201117111259.

[18] Y. Han, P. Kral, Computational design of ACE2-based peptide inhibitors of SARS-CoV-2, ACS Nano. 14 (2020) 5143–5147, https://doi.org/10.1021/acsnano.0c02857.

[19] Y. Wu, F. Wang, C. Shen, W. Peng, D. Li, C. Zhao, et al., A noncompeting pair of human neutralizing antibodies block COVID-19 virus binding to its receptor ACE2, Science 368 (2020) 1274–1278, https://doi.org/10.1126/science.abc2241.

[20] X. Chi, R. Yan, J. Zhang, G. Zhang, Y. Zhang, M. Hao, et al., A neutralizing human antibody binds to the N-terminal domain of the spike protein of SARS-CoV-2, Science 369 (2020) 650–655, https://doi.org/10.1126/science.abc6952.

[21] L. Liu, P. Wang, M.S. Nair, J. Yu, M. Rapp, Q. Wang, et al., Potent neutralizing antibodies against multiple epitopes on SARS-CoV-2 spike, Nature 584 (2020) 450–456, https://doi.org/10.1038/s41586-020-2571-7.

[22] R. Shi, C. Shan, X. Duan, Z. Chen, P. Liu, J. Song, et al., A human neutralizing antibody targets the receptor-binding site of SARS-CoV-2, Nature 584 (2020) 120–124, https://doi.org/10.1038/s41586-020-2381-y.

[23] M. Behbahanipour, R. Benoit, S. Navarro, S. Ventura, OligoBinders: bioengineered soluble amyloid-like nanoparticles to bind and neutralize SARS-CoV-2, ACS Appl. Mater Interfaces. 15 (2023) 11444–11457, https://doi.org/10.1021/acsami.2c18305.

[24] A. Aleem, A.B. Akbar Samad, S. Vaqar, Emerging Variants of SARS-CoV-2 and Novel Therapeutics Against Coronavirus (COVID-19), StatPearls, Treasure Island (FL), 2023, https://www.ncbi.nlm.nih.gov/pubmed/34033342.

[25] W. Zhou, W. Wang, Fast-spreading SARS-CoV-2 variants: challenges to and new design strategies of COVID-19 vaccines, Signal Transduct. Target Ther. 6 (2021) 226, https://doi.org/10.1038/s41392-021-00644-x.

[26] S. Behzadinasab, A. Chin, M. Hosseini, L. Poon, W.A. Ducker, A surface coating that rapidly inactivates SARS-CoV-2, ACS Appl. Mater Interfaces. 12 (2020) 34723–34727, https://doi.org/10.1021/acsami.0c11425.

[27] P.D. Rakowska, M. Tiddia, N. Faruqui, C. Bankier, Y.W. Pei, A.J. Pollard, et al., Antiviral surfaces and coatings and their mechanisms of action, Communications Mater. 2 (2021), https://doi.org/10.1038/s43246-021-00153-y.

[28] A.L. Kubo, G. Vasiliev, H. Vija, J. Krishtal, V. Tougu, M. Visnapuu, et al., Surface carboxylation or PEGylation decreases CuO nanoparticles' cytotoxicity to human cells in vitro without compromising their antibacterial properties, Arch. Toxicol. 94 (2020) 1561–1573, https://doi.org/10.1007/s00204-020-02720-7.

[29] R.H. Bianculli, J.D. Mase, M.D. Schulz, Antiviral polymers: past approaches and future possibilities, Macromolecules 53 (2020) 9158–9186, https://doi.org/10.1021/acs.macromol.0c01273.

[30] J.A. Lemire, J.J. Harrison, R.J. Turner, Antimicrobial activity of metals: mechanisms, molecular targets and applications, Nat. Rev. Microbiol. 11 (2013) 371–384, https://doi.org/10.1038/nrmicro3028.

[31] E. Oliveira, H.M. Santos, J. Garcia-Pardo, M. Diniz, J. Lorenzo, B. Rodríguez-González, et al., Synthesis of functionalized fluorescent silver nanoparticles and their toxicological effect in aquatic environments (Goldfish) and HEPG2 cells, Front. Chem. 1 (2013), https://doi.org/10.3389/fchem.2013.00029.

[32] S. Navarro, M. Diaz-Caballero, F. Peccati, L. Roldan-Martin, M. Sodupe, S. Ventura, Amyloid fibrils formed by short prion-inspired peptides are metalloenzymes, ACS Nano. 17 (2023) 16968–16979, https://doi.org/10.1021/acsnano.3c04164.

[33] T.P. Knowles, R. Mezzenga, Amyloid fibrils as building blocks for natural and artificial functional materials, Adv. Mater. 28 (2016) 6546–6561, https://doi.org/10.1002/adma.201505961.

[34] M. Diaz-Caballero, S. Navarro, I. Fuentes, F. Teixidor, S. Ventura, Minimalist prion-inspired polar self-assembling peptides, ACS Nano. 12 (2018) 5394–5407, https://doi.org/10.1021/acsnano.8b00417.

[35] S. Das, R.S. Jacob, K. Patel, N. Singh, S.K. Maji, Amyloid fibrils: versatile biomaterials for cell adhesion and tissue engineering applications, Biomacromolecules 19 (2018) 1826–1839, https://doi.org/10.1021/acs.biomac.8b00279.

[36] M. Díaz-Caballero, S. Navarro, M. Nuez-Martínez, F. Peccati, L. Rodríguez-Santiago, M. Sodupe, et al., pH-responsive self-assembly of amyloid fibrils for dual hydrolase-oxidase reactions, ACS Catal. 11 (2021) 595–607, https://doi.org/10.1021/acscatal.0c03093.

[37] J. Garcia-Pardo, S. Ventura, Cryo-EM structures of functional and pathological amyloid ribonucleoprotein assemblies, Trends. Biochem. Sci. (2023), https://doi.org/10.1016/j.tibs.2023.10.005.

[38] J. Garcia-Pardo, A. Bartolome-Nafria, A. Chaves-Sanjuan, M. Gil-Garcia, C. Visentin, M. Bolognesi, et al., Cryo-EM structure of hnRNPDL-2 fibrils, a functional amyloid associated with limb-girdle muscular dystrophy D3, Nat. Commun. 14 (2023) 239, https://doi.org/10.1038/s41467-023-35854-0.

[39] T.R. Jahn, O.S. Makin, K.L. Morris, K.E. Marshall, P. Tian, P. Sikorski, L.C. Serpell, The common architecture of cross-beta amyloid, J. Mol. Biol. 395 (2010) 717–727, https://doi.org/10.1016/j.jmb.2009.09.039.

[40] T.P. Knowles, A.W. Fitzpatrick, S. Meehan, H.R. Mott, M. Vendruscolo, C. M. Dobson, M.E. Welland, Role of intermolecular forces in defining material properties of protein nanofibrils, Science 318 (2007) 1900–1903, https://doi.org/10.1126/science.1150057.

[41] A.K. Buell, Stability matters, too - the thermodynamics of amyloid fibril formation, Chem. Sci. 13 (2022) 10177–10192, https://doi.org/10.1039/d1sc06782f.

[42] W. Wang, S. Navarro, R.A. Azizyan, M. Bano-Polo, S.A. Esperante, A.V. Kajava, S. Ventura, Prion soft amyloid core driven self-assembly of globular proteins into bioactive nanofibrils, Nanoscale 11 (2019) 12680–12694, https://doi.org/10.1039/c9nr01755k.

[43] W. Wang, M. Gil-Garcia, S. Ventura, Dual antibody-conjugated amyloid nanorods to promote selective cell-cell interactions, ACS Appl. Mater Interfaces. 13 (2021) 14875–14884, https://doi.org/10.1021/acsami.0c21996.

[44] W. Wang, R.A. Azizyan, A. Garro, A.V. Kajava, S. Ventura, Multifunctional amyloid oligomeric nanoparticles for specific cell targeting and drug delivery, Biomacromolecules 21 (2020) 4302–4312, https://doi.org/10.1021/acs.biomac.0c01103.

[45] L. Cao, I. Goreshnik, B. Coventry, J.B. Case, L. Miller, L. Kozodoy, et al., De novo design of picomolar SARS-CoV-2 miniprotein inhibitors, Science 370 (2020) 426–431, https://doi.org/10.1126/science.abd9909.

[46] J.B. Case, R.E. Chen, L. Cao, B. Ying, E.S. Winkler, M. Johnson, et al., Ultrapotent miniproteins targeting the SARS-CoV-2 receptor-binding domain protect against infection and disease, Cell Host Microbe. 29 (2021) 1151–1161, https://doi.org/10.1016/j.chom.2021.06.008 (e1155).

[47] R. Chattaraj, C.Y. Kim, D. Lee, D.A. Hammer, Recombinant protein micelles to block transduction by SARS-CoV-2 pseudovirus, ACS Nano 16 (2022) 17466–17477, https://doi.org/10.1021/acsnano.2c09015.

[48] Y. Zhu, M. Li, N. Liu, T. Wu, X. Han, G. Zhao, Y. He, Development of highly effective LCB1-based lipopeptides targeting the spike receptor-binding motif of SARS-CoV-2, Antiviral Res. 211 (2023) 105541, https://doi.org/10.1016/j.antiviral.2023.105541.

[49] GraphPad Prism version 10.0.0 for Windows, GraphPad Software, Boston, Massachusetts USA, www.graphpad.com.

[50] M. Mirdita, K. Schütze, Y. Moriwaki, L. Heo, S. Ovchinnikov, M. Steinegger, ColabFold: making protein folding accessible to all, Nat. Methods 19 (2022) 679-+, https://doi.org/10.1038/s41592-022-01488-1.
[51] E.C. Meng, T.D. Goddard, E.F. Pettersen, G.S. Couch, Z.J. Pearson, J.H. Morris, T. E. Ferrin, U.C.S.F. ChimeraX, Tools for structure building and analysis, Protein Sci. 32 (2023), https://doi.org/10.1002/pro.4792.
[52] A. Sali, T.L. Blundell, Comparative protein modelling by satisfaction of spatial restraints, J. Mol. Biol. 234 (1993) 779–815, https://doi.org/10.1006/jmbi.1993.1626.
[53] S. Pronk, S. Páll, R. Schulz, P. Larsson, P. Bjelkmar, R. Apostolov, et al., GROMACS 4.5: a high-throughput and highly parallel open source molecular simulation toolkit, Bioinformatics 29 (2013) 845–854, https://doi.org/10.1093/bioinformatics/btt055.
[54] D.A. Case, H.M. Aktulga, K. Belfon, D.S. Cerutti, G.A. Cisneros, V.W.D. Cruzeiro, et al., The AMBERTOOLs, J. Chem. Inf. Model. (2023), https://doi.org/10.1021/acs.jcim.3c01153.
[55] R.A. Laskowski, M.W. Macarthur, D.S. Moss, J.M. Thornton, Procheck - a program to check the stereochemical quality of protein structures, J. Appl. Cryst. 26 (1993) 283–291, https://doi.org/10.1107/S0021889892009944.
[56] T. Maculins, J. Garcia-Pardo, A. Skenderovic, J. Gebel, M. Putyrski, A. Vorobyov, et al., Discovery of protein-protein interaction inhibitors by integrating protein engineering and chemical screening platforms, Cell Chem. Biol. 27 (2020) 1441–1451 e1447, https://doi.org/10.1016/j.chembiol.2020.07.010.
[57] F. Nador, K. Wnuk, J. García-Pardo, J. Lorenzo, R. Solorzano, D. Ruiz-Molina, F. Novio, Dual-fluorescent nanoscale coordination polymers via a mixed-ligand synthetic strategy and their use for multichannel imaging, ChemNanoMat. 4 (2018) 183–193, https://doi.org/10.1002/cnma.201700311.
[58] J. Garcia-Pardo, R. Grana-Montes, M. Fernandez-Mendez, A. Ruyra, N. Roher, F. X. Aviles, et al., Amyloid formation by human carboxypeptidase D transthyretin-like domain under physiological conditions, J. Biol. Chem. 289 (2014) 33783–33796, https://doi.org/10.1074/jbc.M114.594804.
[59] M. Diaz-Caballero, M.R. Fernandez, S. Navarro, S. Ventura, Prion-based nanomaterials and their emerging applications, Prion 12 (2018) 266–272, https://doi.org/10.1080/19336896.2018.1521235.
[60] M. Diaz-Caballero, S. Navarro, S. Ventura, Functionalized prion-inspired amyloids for biosensor applications, Biomacromolecules 22 (2021) 2822–2833, https://doi.org/10.1021/acs.biomac.1c00222.
[61] J. Li, F. Zhang, Amyloids as building blocks for macroscopic functional materials: designs, applications and challenges, Int. J. Mol. Sci. 22 (2021), https://doi.org/10.3390/ijms221910698.
[62] M.S. Rubel, S.A. Fedotov, A.V. Grizel, J.V. Sopova, O.A. Malikova, Y.O. Chernoff, A.A. Rubel, Functional mammalian amyloids and amyloid-like proteins, Life (Basel). 10 (2020), https://doi.org/10.3390/life10090156.
[63] D. Willbold, B. Strodel, G.F. Schroder, W. Hoyer, H. Heise, Amyloid-type protein aggregation and prion-like properties of amyloids, Chem. Rev. 121 (2021) 8285–8307, https://doi.org/10.1021/acs.chemrev.1c00196.
[64] C. Seuring, J. Verasdonck, P. Ringler, R. Cadalbert, H. Stahlberg, A. Bockmann, et al., Amyloid fibril polymorphism: almost identical on the atomic level, mesoscopically very different, J. Phys. Chem. B. 121 (2017) 1783–1792, https://doi.org/10.1021/acs.jpcb.6b10624.
[65] W. Close, M. Neumann, A. Schmidt, M. Hora, K. Annamalai, M. Schmidt, et al., Physical basis of amyloid fibril polymorphism, Nat. Commun. 9 (2018) 699, https://doi.org/10.1038/s41467-018-03164-5.
[66] S. Lovestam, D. Li, J.L. Wagstaff, A. Kotecha, D. Kimanius, S.H. McLaughlin, et al., Disease-specific tau filaments assemble via polymorphic intermediates, Nature (2023), https://doi.org/10.1038/s41586-023-06788-w.
[67] E. Tayeb-Fligelman, O. Tabachnikov, A. Moshe, O. Goldshmidt-Tran, M.R. Sawaya, N. Coquelle, et al., The cytotoxic Staphylococcus aureus PSMα3 reveals a cross-α amyloid-like fibril, Science 355 (2017) 831–833, https://doi.org/10.1126/science.aaf4901.
[68] N. Salinas, E. Tayeb-Fligelman, M.D. Sammito, D. Bloch, R. Jelinek, D. Noy, et al., The amphibian antimicrobial peptide uperin 3.5 is a cross-α/cross-β chameleon functional amyloid, Proc. Natl. Acad. Sci. 118 (2021) e2014442118, https://doi.org/10.1073/pnas.2014442118.
[69] R. Sant'Anna, M.R. Fernandez, C. Batlle, S. Navarro, N.S. de Groot, L. Serpell, S. Ventura, Characterization of amyloid cores in prion domains, Sci. Rep. 6 (2016) 34274, https://doi.org/10.1038/srep34274.
[70] A.E. Badaczewska-Dawid, J. Garcia-Pardo, A. Kuriata, J. Pujols, S. Ventura, S. Kmiecik, A3D database: structure-based predictions of protein aggregation for the human proteome, Bioinformatics 38 (2022) 3121–3123, https://doi.org/10.1093/bioinformatics/btac215.
[71] A.E. Badaczewska-Dawid, A. Kuriata, C. Pintado-Grima, J. Garcia-Pardo, M. Burdukiewicz, V. Iglesias, et al., A3D model organism database (A3D-MODB): a database for proteome aggregation predictions in model organisms, Nucleic Acids Res. (2023), https://doi.org/10.1093/nar/gkad942.
[72] J. Garcia-Pardo, A.E. Badaczewska-Dawid, C. Pintado-Grima, V. Iglesias, A. Kuriata, S. Kmiecik, S. Ventura, A3DyDB: exploring structural aggregation propensities in the yeast proteome, Microb. Cell Fact. 22 (2023) 186, https://doi.org/10.1186/s12934-023-02182-3.
[73] V. Castillo, S. Ventura, Amyloidogenic regions and interaction surfaces overlap in globular proteins related to conformational diseases, PLoS Comput. Biol. 5 (2009) e1000476, https://doi.org/10.1371/journal.pcbi.1000476.
[74] A. Kuriata, V. Iglesias, J. Pujols, M. Kurcinski, S. Kmiecik, S. Ventura, Aggrescan3D (A3D) 2.0: prediction and engineering of protein solubility, Nucleic Acids Res. 47 (2019) W300–W307, https://doi.org/10.1093/nar/gkz321.
[75] T.A. Belashova, A.A. Valina, E.I. Sysoev, M.E. Velizhanina, A.A. Zelinsky, A. P. Galkin, Search and identification of amyloid proteins, Methods and Protocols. 6 (2023) 16, https://doi.org/10.3390/mps6010016.
[76] B.H. Toyama, J.S. Weissman, Amyloid structure: conformational diversity and consequences, Annu. Rev. Biochem. 80 (2011) 557–585, https://doi.org/10.1146/annurev-biochem-090908-120656.
[77] L. Schrödinger, W. DeLano, The PyMOL Molecular Graphics System, Schrödinger, LLC, 2020.
[78] V. Novitskaya, O.V. Bocharova, I. Bronstein, I.V. Baskakov, Amyloid fibrils of mammalian prion protein are highly toxic to cultured cells and primary neurons, J. Biol. Chem. 281 (2006) 13828–13836, https://doi.org/10.1074/jbc.M511174200.
[79] M. Bucciantini, D. Nosi, M. Forzan, E. Russo, M. Calamai, L. Pieri, et al., Toxic effects of amyloid fibrils on cell membranes: the importance of ganglioside GM1, FASEB J. 26 (2012) 818–831, https://doi.org/10.1096/fj.11-189381.
[80] R. Cascella, A. Bigi, N. Cremades, C. Cecchi, Effects of oligomer toxicity, fibril toxicity and fibril spreading in synucleinopathies, Cell Mol. Life Sci. 79 (2022) 174, https://doi.org/10.1007/s00018-022-04166-9.
[81] A. Reyes-Alcaraz, E.Y. Lucero Garcia-Rojas, E.A. Merlinsky, J.Y. Seong, R.A. Bond, B.K. McConnell, A NanoBiT assay to monitor membrane proteins trafficking for drug discovery and drug development, Commun. Biol. 5 (2022) 212, https://doi.org/10.1038/s42003-022-03163-9.
[82] J. Xu, C. Xu, R. Chen, Y. Yin, Z. Wang, K. Li, et al., Stability of SARS-CoV-2 on inanimate surfaces: a review, Microbiol. Res. 272 (2023) 127388, https://doi.org/10.1016/j.micres.2023.127388.
[83] Y. Geng, Y. Wang, Stability and transmissibility of SARS-CoV-2 in the environment, J. Med. Virol. 95 (2023) e28103, https://doi.org/10.1002/jmv.28103.
[84] T. Bierig, G. Collu, A. Blanc, E. Poghosyan, R.M. Benoit, Design, expression, purification, and characterization of a YFP-tagged 2019-nCoV spike receptor-binding domain construct, Front. Bioeng. Biotechnol. 8 (2020) 618615, https://doi.org/10.3389/fbioe.2020.618615.
[85] M.C. Sportelli, M. Izzi, E.A. Kukushkina, S.I. Hossain, R.A. Picca, N. Ditaranto, N. Cioffi, Can nanotechnology and materials science help the fight against SARS-CoV-2? Nanomaterials (Basel). 10 (2020) https://doi.org/10.3390/nano10040802.